Highlights

Dynamics in a Low-Rank Separable Field Cellular Automaton

Xiaorui Shi, Mengsha Huang

- A normalized separable-field cellular automaton produces extinction, fixed points, cycles, and long transients.
- Survival-birth interval geometry organizes the phase diagram.
- Long transients form a narrow ridge between two cyclic attractor basins with distinct fingerprints.
- Sparse stripe-like cycles explain why wider survival intervals can produce lower final density.

Dynamics in a Low-Rank Separable Field Cellular Automaton

Xiaorui Shi[a,*,1], Mengsha Huang[b,*,1]

[a] Weixian College, Tsinghua University, Beijing, China
[b] Department of Physics, Tsinghua University, Beijing, China

ARTICLE INFO

Keywords:
cellular automata
long transients
attractor basins
phase diagram
damage spreading
normalized field

ABSTRACT

Cellular automata (CA), a series of computational models used to study the emergence of life-like behaviors, classically apply local interaction and updating rules. Yet, another interacting paradigm observed in life, the globally coupled computation is usually overlooked in traditional CA. Here, we introduce a Separable-Field Cellular Automaton (SFCA), a normalized-field cellular automaton in which local-neighborhood interactions is replaced by cell-updating rules governed by a global coupling field. Each cell is updated according to a normalized field $q = n/n_{\max}$, with survival and birth governed by two threshold intervals, $\mathcal{S}$ and $\mathcal{B}$. Systematic scans over interval widths and positions revealed four outcome classes: extinction, fixed points, cycles, and long transients. The outcome phase diagram was organized by the relative geometry of the survival and birth intervals: fixed points dominated when $\mathcal{B}$ was contained in $\mathcal{S}$, whereas long transients concentrated near the boundary between partial overlap and no overlap. A fine scan along this transition showed that the long-transient region forms a narrow but persistent ridge separating two qualitatively distinct cycle-dominated regimes. One side produced dense, high-change-rate cycles approximating global period-2 alternation, whereas the other produced sparse, low-change-rate, stripe-like cycles. Damage-spreading further supported a basin-competition interpretation, in which the long-transient ridge reflects delayed selection between two cyclic attractor families rather than random nonconvergence, while finite-size analysis shows that the long-transient ridge remains robust across tested grid sizes. These results illustrate that long-transient dynamics can arise under separable field coupling with a rank-1 field matrix, suggesting that nontrivial collective organization does not necessarily require complicated interaction rules in a globally coupled system.

1. Introduction

A central question in artificial life lies in whether complex collective organization requires complex interactions. Classical cellular automata (CA), a series of computational models long being used to study the emergence of life-like behaviors, involve discrete, often binary, cells, and usually local interacting and updating rules. Specifically, Conway's Game of Life illustrates that standard local Moore interactions can produce fixed structures, oscillations, propagating patterns, and prolonged transients (Gardner (1970), Wolfram (1984), Crutchfield and Kaneko (1988)). Besides, growing neural cellular automata have been proposed, which prove that parameters in local updating rules can be trained to generate engineered global patterns (Mordvintsev, Randazzo, Niklasson and Levin (2020), Pajouheshgar, Xu, Abbasi, Mordvintsev, Jakob and Süsstrunk (2025)). These have implied that organized dynamical behaviors or global pattern formation and restoration can be realized by simple local-neighborhood interactions.

Nevertheless, the complexity of life arises from multiple paradigms more than just local interactions, while globally coupled, computation-like dynamics also play an essential role. For instance, engineered protein dimerization networks have been shown to perform decision-making computations, with a network's classification output encoded in the steady-state concentrations and mutual affinities of individual monomers (Parres-Gold, Levine, Emert, Stuart and Elowitz (2025)). In the brain, synaptic normalization operates as a global constraint that scales synaptic weights across a neuronal population—a process critical for learning and other complex functions (Mayzel and Schneidman (2024)). These examples point toward a field-like computational paradigm: each component contributes to a shared, system-level field that, in turn, feeds back to update the states of the components.

Thus, we propose a novel computational model to investigate whether long-lived dynamics can arise in a CA whose cell-updating rules are governed by a global field, rather than by the states of its local Moore neighborhood.

*Co-corresponding authors: Xiaorui Shi and Mengsha Huang.
xs326@cantab.ac.uk (X. Shi); huangms22@outlook.com (M. Huang)
ORCID(s):
[1] Xiaorui Shi and Mengsha Huang contributed equally to this work and share first authorship.

Here, the global field matrix is deliberately reduced to an extremely low-rank form, imposing a stringent constraint on the system's degrees of freedom. Our coupling rule is inspired by Kauffman's autocatalytic-set perspective, which posits that collective organization can emerge from the joint action of distributed catalytic relations rather than from a central controller (Kauffman (1986), JD (1986)). Such catalytic function may, in turn, arise from the affinity between atomic groups on substrates and catalysts, with distinct group-pairs contributing in a separable manner. We abstract and simplify this idea using two coarse-grained affinity factors and, under a separability assumption, represent their joint contribution by a product. Taking the row and column activity profiles as these two factors yields the instantaneous field matrix has rank at most one, as it is formed by the outer product of two vectors. This construction defines the Separable-Field Cellular Automaton (SFCA). It is not intended as a literal model of autocatalytic chemistry, but as a minimal dynamical abstraction of multi-factor compatibility under rank-one coupling.

We ask how the geometry of the survival and birth intervals organizes the long-term dynamics of this system. Systematic scans reveal extinction, fixed points, cycles, and long transients in distinct regions of parameter space. Fixed points are enriched when the birth interval is contained within the survival interval, whereas long transients form a narrow ridge near the boundary between partial overlap and no overlap. This ridge separates a dense, rapidly alternating cycle regime from a sparse, stripe-like, low-change-rate cycle regime, consistent with a possible delayed selection between two cyclic attractor families. The SFCA therefore provides a minimal model in which rank-one field coupling generates prolonged dynamics organized by survival–birth interval geometry.

2. Model and methods

2.1. Separable-field update rule

The system is a binary cellular automaton on a periodic $H \times W$ lattice. The state at generation t is denoted by $X_t(j,i) \in \{0,1\}$, where 1 indicates an alive cell. Instead of counting the Moore neighborhood of each cell, the model first computes the column and row occupancies

$$c_i(t) = \sum_{j=1}^{H} X_t(j,i), \qquad r_j(t) = \sum_{i=1}^{W} X_t(j,i). \tag{1}$$

These one-dimensional sums are locally blurred using nearest-neighbor periodic wrapping,

$$C_i(t) = c_{i-1}(t) + c_i(t) + c_{i+1}(t), \qquad R_j(t) = r_{j-1}(t) + r_j(t) + r_{j+1}(t), \tag{2}$$

and the unnormalized field at cell (j,i) is defined as

$$n_t(j,i) = R_j(t) C_i(t). \tag{3}$$

The field is then normalized by its lattice maximum,

$$q_t(j,i) = \frac{n_t(j,i)}{n_{\max}(t)}, \qquad n_{\max}(t) = \max_{j,i} n_t(j,i), \tag{4}$$

with the convention that an all-dead lattice remains all dead.

Two closed intervals determine the synchronous update rule. An alive cell survives if $q_t(j,i) \in \mathcal{S} = [S_{\text{low}}, S_{\text{high}}]$, while a dead cell is born if $q_t(j,i) \in \mathcal{B} = [B_{\text{low}}, B_{\text{high}}]$. Thus

$$X_{t+1}(j,i) = \begin{cases} 1, & X_t(j,i) = 1 \text{ and } q_t(j,i) \in \mathcal{S}, \\ 1, & X_t(j,i) = 0 \text{ and } q_t(j,i) \in \mathcal{B}, \\ 0, & \text{otherwise.} \end{cases} \tag{5}$$

The normalization by $n_{\max}$ is essential: the same absolute configuration can become more or less permissive depending on how strongly the current pattern concentrates the field.

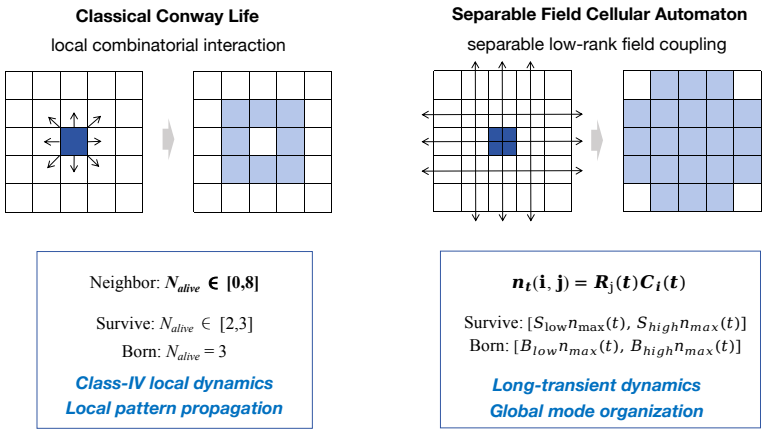

Figure 1: Comparison between Classical Conway Life and the Separable Field Cellular Automaton (SFCA). Conway Life is a classical local cellular automaton in which each cell updates based on the number of alive neighbors in its 3×3 neighborhood. Cells survive if they have 2–3 alive neighbors and are born with exactly 3 neighbors. This produces Class-IV local dynamics with localized pattern propagation, including gliders, oscillators, and still lifes. The Separable Field Cellular Automaton (SFCA) updates each cell according to a rank-1 separable row-column interaction field, $n_t(i,j) = R_j(t)C_i(t)$. Survival and birth are determined relative to the normalized field ($[S_{low}n_{max}(t), S_{high}n_{max}(t)]$ for survival; $[B_{low}n_{max}(t), B_{high}n_{max}(t)]$ for birth). The SFCA exhibits long-transient dynamics and global mode organization.

2.2. Parameterization of survival and birth intervals

For the coarse scans, endpoints were placed on an 18-level grid. The survival and birth widths were

$$w_S = S_{\text{high}} - S_{\text{low}}, \qquad w_B = B_{\text{high}} - B_{\text{low}}. \tag{6}$$

In the width-only scan, every pair (w_S, w_B) was averaged over all legal interval positions satisfying $S_{\text{low}} < B_{\text{low}}$. In geometry-focused scans, we fixed the offset

$$\Delta_{\text{low}} = B_{\text{low}} - S_{\text{low}} \tag{7}$$

and used the two boundaries $B_{\text{high}} = S_{\text{high}}$ and $B_{\text{low}} = S_{\text{high}}$ to divide the plane into three interval-geometric regions: $\mathcal{B} \subseteq \mathcal{S}$, partial overlap, and no overlap.

For the fine transition scan, endpoints were placed on a 180-level grid. Unless otherwise stated, we used $S_{\text{low}} = 10/180 = 1/18$ and $\mathcal{B} = [60/180, 160/180] = [6/18, 16/18]$, and varied w_S along the transition axis. This axis crosses the long-transient ridge observed in the coarse phase diagram while keeping the birth interval fixed.

2.3. Simulation protocol and outcome classification

Initial states were independent Bernoulli random lattices with density $\rho_0 = 0.25$, except in the initial-density control experiment where ρ_0 was varied from 0.05 to 0.95. Most scans used a 75×100 lattice. Coarse scans were run for 2000 generations. Fine transition and survival analyses were run for up to 100,000 generations. A full-history hash buffer was used to detect repeated states during each run.

Each trajectory was assigned to one of four outcome classes. Extinction was recorded when all cells were dead. A fixed point was recorded when the state repeated with period 1. A cycle was recorded when a previous state repeated with period at least 2. A long transient was recorded when the maximum generation did not detect an extinction, fixed point, or cycle. The long-transient class should therefore be interpreted as "not observed to terminate within the specified observation window", not as proof of non-periodicity for infinite time.

2.4. Dynamical measurements

To characterize attractor dynamics, we measured density, change rate, stripe score, and damage spreading. The density is

$$\rho(t) = \frac{1}{HW} \sum_{j,i} X_t(j,i), \tag{8}$$

and the change rate is

$$\chi(t) = \frac{1}{HW} \sum_{j,i} \left| X_{t+1}(j,i) - X_t(j,i) \right| . \tag{9}$$

For cycle-class runs, we aggregated the mean density and mean change rate within the detected cycle or over the recorded trajectory after convergence.

The stripe score was designed to detect row- or column-aligned spatial heterogeneity. For a lattice X, let $\bar{X}_{j\cdot}$ be the mean of row j and $\bar{X}_{\cdot i}$ the mean of column i. We define

$$\sigma_{\text{stripe}}(X) = \text{Var}_j(\bar{X}_{j\cdot}) + \text{Var}_i(\bar{X}_{\cdot i}). \tag{10}$$

A homogeneous dense cycle has a low stripe score even when many cells flip, whereas a banded or stripe-like sparse pattern has a higher stripe score.

For damage spreading, paired trajectories were initialized from nearly identical states with only one cell's difference, and compared using the normalized Hamming distance

$$d_H(t) = \frac{1}{HW} \sum_{j,i} |X_t(j,i) - Y_t(j,i)|. \tag{11}$$

We further computed a finite-time effective perturbation-growth rate,

$$\lambda_{\text{eff}}(t) = \frac{1}{t} log(\frac{\tilde{d}_H(t)}{\tilde{d}_H(0)}) \tag{12}$$

This quantify measures the average exponential rate of perturbation amplification between the initial condition and generation t, rather than an asymptotic Lyapunov exponent.

Phase-shift and translation controls were used to test whether large distances could be explained by the same cycle observed at different phases or by spatially shifted versions of similar patterns.

3. Results

3.1. A single SFCA rule can support all four outcome classes

Before scanning the full parameter space, we first verified that the SFCA can support multiple long-term outcomes under a single rule. For the representative rule $\mathcal{S} = [3/18, 11/18]$ and $\mathcal{B} = [7/18, 9/18]$, 100,000 independent random initial states yielded all four outcome classes within a 2000-generation window: 16.70% extinction, 3.99% cycle, 15.99% long transient, and 63.32% fixed point. Representative snapshots show that these outcomes are visually distinct despite sharing the same rule parameters (Fig. 2).

3.2. A global parameter scan reveals four dynamical regimes

We next scanned the phase diagram using w_S and w_B as the two axes. For each width pair, all legal interval positions satisfying $S_{\text{low}} < B_{\text{low}}$ were sampled, and 1000 trajectories for each width combination were simulated on a 75×100 grid for 2000 generations. When certain width combination include more than one group of $S_{\text{low}}, S_{\text{high}}, B_{\text{low}}, B_{\text{high}}$ combinations, the trajectories were evenly distributed among each group. The resulting four-class outcome heatmaps showed a strongly organized phase diagram rather than a monotonic response to interval width (Fig. 3). Extinction was concentrated near the lower-left corner, where both survival and birth intervals were narrow. Fixed points dominated when the survival interval was wide and the birth interval was narrow. Cycle-rich regions occupied broad bands outside this fixed-point domain, while long transients appeared primarily as intermediate transition regions.

The outcome maxima emphasize this organization. In the width-only scan, extinction reached 88.3% at the smallest survival and birth widths. Cycle share reached 100% in a wide-birth, narrow-survival region. Long-transient share reached 57.0% in the interior transition band. Fixed-point share reached 95.0% in a wide-survival, narrow-birth region. These observations suggest that the balance between survival permissiveness and birth permissiveness is not sufficient by itself; the relative placement of $\mathcal{S}$ and $\mathcal{B}$ must also be considered.

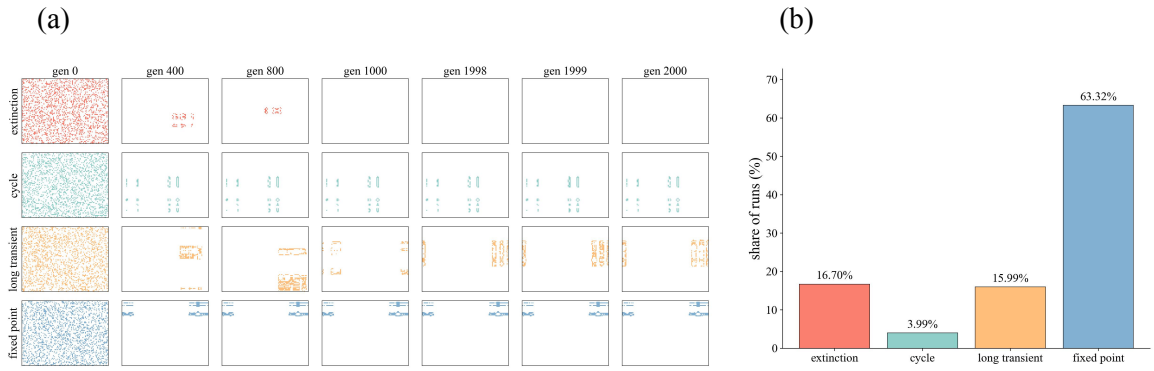

Figure 2: Representative outcome classes under a single SFCA rule. (a) Example trajectories leading to extinction, fixed point, cycle, and long transient under $\mathcal{S} = [3/18, 11/18]$ and $\mathcal{B} = [7/18, 9/18]$. Each row shows snapshots from an independent random initialization at generations 0, 400, 800, 1000, 1998, 1999, and 2000. Dark green cells indicate alive cells and light green cells indicate dead cells. The extinction example reaches the all-dead state by generation 825; the fixed-point example reaches a static state by generation 275; the cycle example enters a period-2 orbit by generation 132; and the long-transient example remains unclassified within the 2000-generation observation window. (b) Outcome composition from 100,000 independent random initializations under the same rule. The same parameter setting can generate extinction, fixed points, cycles, and long transients depending on the initial condition.

3.3. Survival-birth interval geometry organizes the phase diagram

To isolate interval geometry from width alone, we fixed $\Delta_{\text{low}} = B_{\text{low}} - S_{\text{low}}$. For $\Delta_{\text{low}} = 5/18$, the boundaries $B_{\text{low}} = S_{\text{high}}$ and $B_{\text{high}} = S_{\text{high}}$ divide the width plane into no-overlap, partial-overlap, and $\mathcal{B} \subseteq \mathcal{S}$ regions. This geometric decomposition captured two major features of the phase diagram (Fig. 3b). First, the $\mathcal{B} \subseteq \mathcal{S}$ region was enriched for fixed points, consistent with the idea that cells born under $\mathcal{B}$ are then likely to satisfy the survival condition. Second, long transients were concentrated near the boundary where the upper edge of the survival interval approaches the lower edge of the birth interval.

This geometry initially explains why the long-transient region separates two cycle-rich domains. When S_{high} is below B_{low}, survival and birth are driven by disjoint field ranges. When S_{high} crosses B_{low}, a persistence band appears in which a cell can satisfy both survival and birth conditions depending on its current state. The long-transient ridge lies near this change in rule logic, indicating that delayed convergence is linked to the emergence of competing update mechanisms rather than to random noise in the scan.

3.4. Outcome classes are mostly robust to initial density

A possible alternative explanation is that the observed phase structure is an artifact of the chosen initial density. To test this, we selected anchor rules enriched for extinction, saturation/fixed-point behavior, non-trivial fixed points, cycles, and long transients, and swept the initial density from $\rho_0 = 0.05$ to 0.95. The extinction, cycle, and long-transient anchors retained their dominant outcome over broad density ranges around $\rho_0 = 0.25$ (Fig. 4). For example, the cycle anchor remained cycle-dominated over a strong band from $\rho_0 = 0.05$ to 0.85, and the long-transient anchor remained long-transient-dominated over the same strong band. Fixed-point anchors were more density-sensitive: at high initial density, some fixed-point cases shifted toward extinction.

These controls indicate that the main outcome regions are not merely consequences of a single initial-density choice. Initial density can affect the accessibility of fixed-point states, but the cycle and long-transient transition described below persists under density perturbations around the reference density.

3.5. A persistent long-transient peak separates two cycle-dominated regimes

We then focused on the transition axis $S_{\text{low}} = 10/180$, $\mathcal{B} = [60/180, 160/180]$, scanning $w_{\mathcal{S}}$ at resolution $1/180$. On this axis, extinction and fixed points were absent; the system showed a direct competition between cycles and long transients. In the 100,000-generation scan over $w_{\mathcal{S}} = 45/180$ to $75/180$, cycle share was 100% on both sides of the transition, whereas long-transient share rose sharply between $57/180$ and $64/180$, reaching 97% at $w_{\mathcal{S}} = 61/180$ (Fig. 5 left).

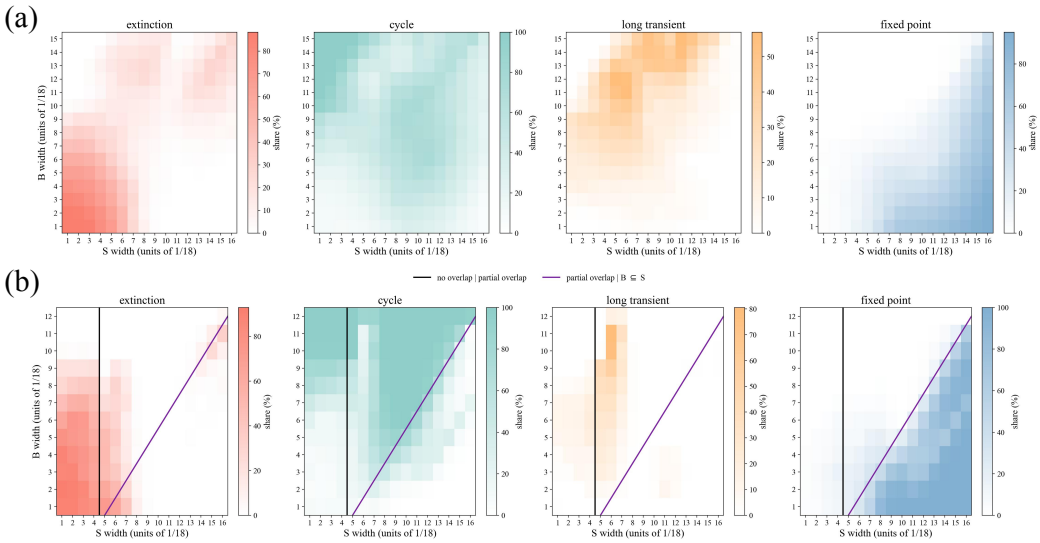

Figure 3: (a)Global outcome phase diagram over survival width w_S and birth width w_B. Each cell averages over legal interval positions and 1000 random initial states. The four panels show the fraction of extinction, cycle, long-transient, and fixed-point outcomes. The scan reveals extinction near narrow intervals, fixed points in wide-survival/narrow-birth regions, and long-transient transition bands that separate cycle-rich regions.(b)Interval geometry for the offset $\Delta_{\text{low}} = 5/18$. The boundary $B_{\text{low}} = S_{\text{high}}$ separates no-overlap from partial-overlap regimes, while $B_{\text{high}} = S_{\text{high}}$ separates partial overlap from $\mathcal{B} \subseteq \mathcal{S}$. Fixed points are enriched where the birth interval is contained within the survival interval, whereas long transients form a transition ridge near the overlap boundary.

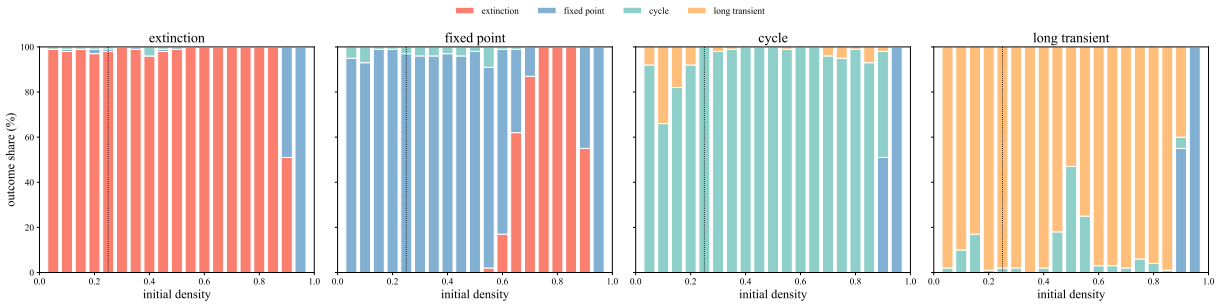

Figure 4: Initial-density control. Outcome composition was measured for anchor rules enriched for different outcome classes while varying ρ_0 from 0.05 to 0.95. Extinction, cycle, and long-transient anchors show broad robustness around $\rho_0 = 0.25$, whereas fixed-point behavior is more sensitive to high initial density.

Kaplan-Meier-style survival curves confirmed that the long-transient window remained visible under longer observation times (Fig. 5 right). At $w_S = 50/180$, $53/180$, $56/180$, $65/180$, and $70/180$, all 1000 runs eventually entered detected cycles by 100,000 generations. In contrast, the middle widths retained substantial censored fractions at the endpoint: 62.5% at $58/180$, 94.7% at $60/180$, and 75.0% at $62/180$. Thus, the long-transient peak is not an artifact of the 2000-generation coarse scan; it marks a region with exceptionally delayed attractor entry.

3.6. The two cycle regions have distinct dynamical fingerprints

Although both sides of the long-transient peak were cycle-dominated, their cycles were not dynamically equivalent. On the low-w_S side, cycle-class runs had high density and high change rate. At $w_S = 55/180$, the mean cycle density was 0.470 ± 0.039 and the mean change rate was 0.997 ± 0.007, indicating almost global alternation between consecutive phases. On the high-w_S side, cycles were sparse and nearly stationary. At $w_S = 70/180$, the mean cycle density was 0.332 ± 0.045 and the mean change rate was 0.027 ± 0.013 (Fig. 6 left).

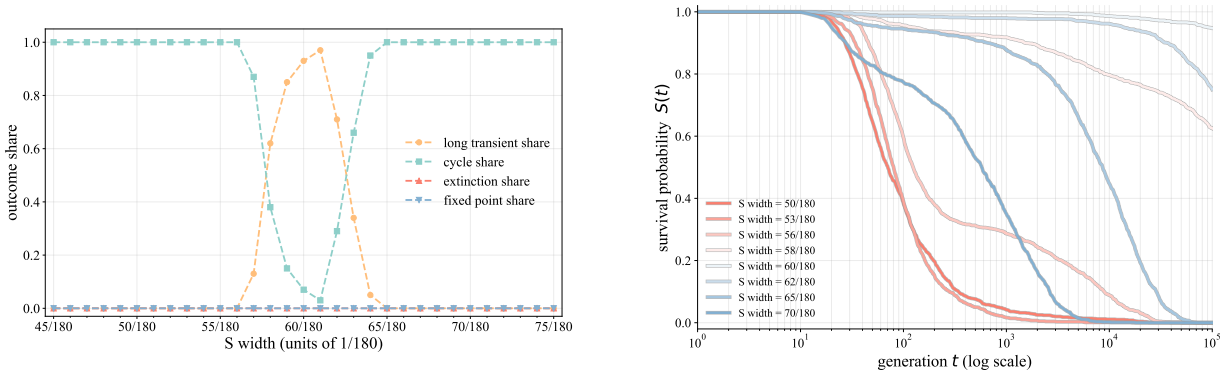

Figure 5: Fine transition scan. Left: Outcome shares along the canonical axis $S_{\text{low}} = 10/180$, $\mathcal{B} = [60/180, 160/180]$. Long transients form a narrow peak between two cycle-dominated plateaus. Right: Kaplan-Meier-style survival curves for selected w_S values, where survival denotes remaining unclassified by extinction, fixed point, or cycle at generation t.

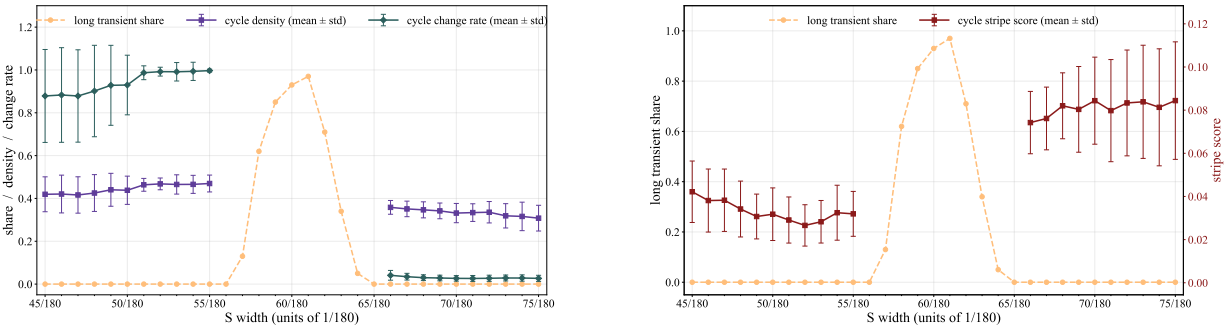

Figure 6: Cycle fingerprints on the two sides of the long-transient window. Left: Cycle density and change rate separate a dense, high-change-rate branch from a sparse, low-change-rate branch. Right: Stripe score is higher in the sparse branch, indicating stronger row/column heterogeneity. Error bars show standard deviation across cycle-class runs. The increased stripe score on the high-w_S side explains why a wider survival interval can nevertheless produce lower global cycle density: localized dense bands raise $n_{\max}$, reducing the relative field $q = n/n_{\max}$ outside those bands.

The decrease in cycle density with increasing survival width is initially counterintuitive. A wider survival interval might be expected to preserve more living cells, yet the high-w_S cycle branch was less dense than the low-w_S branch. The stripe score resolved this paradox. Sparse cycles had substantially higher stripe scores than dense cycles: the score was approximately 0.032 ± 0.010 at $w_S = 55/180$ but 0.084 ± 0.020 at $w_S = 70/180$ (Fig. 6 right). The high-w_S branch therefore does not simply maintain fewer cells uniformly; it organizes cells into heterogeneous stripe-like structures.

Because the update rule uses $q = n/n_{\max}$, such heterogeneity changes the effective field landscape. Dense bands or hotspots raise $n_{\max}$, which lowers the relative field values of cells outside those regions. As a result, high-density regions can remain self-sustaining while low-density regions remain below the birth threshold. Widening the survival interval can therefore stabilize localized structures without increasing the global density. This mechanism distinguishes the sparse, low-change-rate cycle basin from the dense, high-change-rate cycle basin.

3.7. Long transients are consistent with competition between two cycle basins

The combined outcome and fingerprint data support a basin-competition interpretation. The low-w_S cycle branch and high-w_S cycle branch have distinct densities, change rates, and stripe scores, indicating that they are different attractor families rather than two continuous deformations of a single cycle type. The long-transient peak lies between them, precisely where the rule geometry changes from almost disjoint survival and birth ranges to a wider persistence band. We therefore interpret the long-transient ridge as a delayed basin-selection region: trajectories near this boundary do not rapidly commit to either the dense alternating cycle basin or the sparse stripe-like cycle basin.

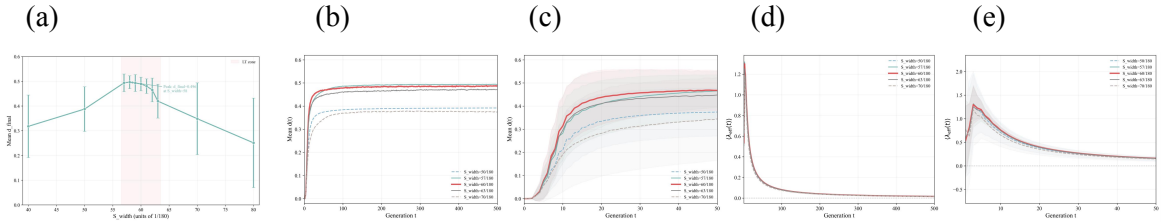

Figure 7: Damage spreading across the long-transient transition. (a) Plateau normalized Hamming distance between paired trajectories initialized from states differing by a single cell, plotted as a function of survival width w_S. The shaded region marks the survival-width range in which long transients are enriched. Hamming separation is lower in the two cycle-dominated regions and increases near the long-transient peak. (b) Representative time courses of $d_H(t)$ for selected w_S values. Perturbations spread rapidly from the one-cell difference and approach width-dependent plateaus. (c) First 50 generations of $d_H(t)$ for selected w_S values. values. (d) Effective finite-time growth rate $\lambda_{\text{eff}}(t)$ computed from changes in $d_H(t)$. The growth rate rises during the early spreading phase but decays toward zero, indicating that the long-transient region does not exhibit sustained exponential divergence. (e) Effective finite-time growth rate $\lambda_{\text{eff}}(t)$ computed from changes in $d_H(t)$ (first 50 generations).

This interpretation also explains why the long-transient peak is narrow. Far from the boundary, one cycle basin dominates and convergence is rapid or moderately delayed. Near the boundary, neither basin fully stabilizes early, and trajectories can wander for long times through states that retain features of both mechanisms. The long-transient class is therefore not an isolated anomaly but a structured transition zone in rule space.

3.8. Damage spreading is enhanced in the long-transient region

We next characterized sensitivity to perturbations using paired-trajectory damage spreading. The plateau Hamming distance was lower in the two cycle-dominated regions and higher near the long-transient peak (Fig.7a). The time-dependent distance $d_H(t)$ rose rapidly from the initial perturbation and then approached a plateau (Fig.7b,c). The corresponding effective growth rate $\lambda_{\text{eff}}(t)$ increased early but decayed toward zero rather than remaining positive indefinitely (Fig.7d,e). These observations indicate that the long-transient region amplifies perturbations to larger separations than the neighboring cycle basins, but it does not behave as a sustained exponentially divergent chaotic regime.

Two controls were used to test whether the elevated Hamming distance was a measurement artifact (Figure S10-S11). First, we compared phases of the same cycle to determine whether $d_H(t)$ was dominated by phase offsets within a periodic orbit. Second, we tested whether similar patterns shifted up, down, left, or right could account for the observed distance. Both contributions were small. Thus, the damage-spreading signal reflects genuine dynamical separation between nearby trajectories rather than trivial phase or translation mismatch.

3.9. Finite-size scans support a robust long-transient window

Finally, we examined whether the long-transient window was tied to a specific grid size (Fig.8). Fine scans were repeated on grids of size 50×37, 100×75, 150×112, and 200×150. The peak long-transient fraction was already high on the smallest grid, reaching approximately 87% within the 100,000-generation window. From 100×75 onward, the peak approached saturation, reaching approximately 97% or higher. The peak position shifted systematically toward smaller w_S as grid size increased.

To relate this size dependence to field organization, we measured the temporal standard deviation of the normalized field $q = n/n_{\max}$ during the first 2000 generations. Across selected widths and grid sizes, the ordering of the normalized-field standard-deviation curves matched the ordering of long-transient fractions. These observations suggest that long-transient behavior is coupled to fluctuations in the normalized field and is not a single-size artifact.

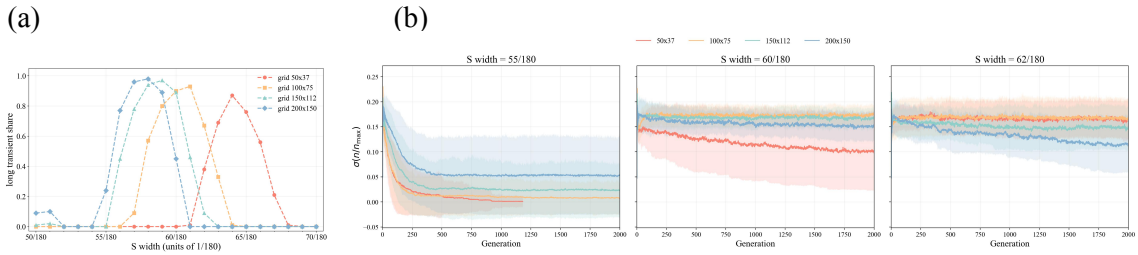

Figure 8: Finite-size behavior of the long-transient window. (a) Long-transient share across the canonical transition axis for grids of size 50×37, 100×75, 150×112, and 200×150. The long-transient peak is present at all tested sizes, increases from the smallest grid to larger grids, and shifts toward smaller w_S as lattice size increases. (b) Temporal standard deviation of the normalized field $q = n/n_{\max}$ during the first 2000 generations for selected survival widths. Across grid sizes, higher normalized-field fluctuations are associated with stronger long-transient enrichment.

4. Discussion

The main result is that long transients in the SFCA are geometrically organized. They arise near specific relationships between the survival and birth intervals, especially near the boundary where S_{high} approaches B_{low}. This finding differs from a view in which long transients are rare stochastic-looking exceptions. In this system, long transients form a coherent ridge in parameter space and are reproducible under independent random initial conditions.

The interval-containment result provides a simple explanation for the fixed-point-rich region. When $\mathcal{B} \subseteq \mathcal{S}$, the field values that allow dead cells to become alive also allow alive cells to remain alive. Once a viable pattern is formed, the rule therefore contains a built-in stabilizing tendency. This does not guarantee convergence to a fixed point from every initial condition, but it explains why fixed points dominate in that geometric region of the phase diagram.

The long-transient ridge is more subtle. Along the canonical transition axis, the ridge separates two cycle branches with sharply different fingerprints. The low-w_S branch behaves like a dense alternating attractor, with nearly all cells flipping each generation. The high-w_S branch behaves like a sparse structured attractor, with only a small fraction of cells changing. Because the long-transient peak lies between these two branches, it is natural to interpret it as a basin-competition region. This interpretation is further supported by the damage-spreading results: trajectories near the ridge separate more strongly than those inside either cycle basin, but the effective growth rate decays toward zero rather than showing sustained exponential divergence.

The density paradox highlights the special role of normalization. In ordinary neighbor-count cellular automata, widening a survival interval would often be interpreted as making survival more permissive. In the SFCA, however, the relevant quantity is not the absolute field but the field divided by $n_{\max}$. Stripe-like structures can increase $n_{\max}$ locally and thereby suppress relative field values elsewhere. The rule can therefore support lower global density even when the survival interval is wider, because the attractor has reorganized the field distribution.

Several limitations remain. First, long transients are defined operationally by a finite observation window. Longer simulations or exact state-space arguments would be needed to distinguish extremely long transients from cycles with periods beyond 100,000 generations. Second, the basin-competition interpretation is supported by outcome shares, cycle fingerprints, and damage spreading, but a direct basin map would provide stronger evidence. Third, finite-size scans show robustness over the tested sizes, yet a more systematic scaling analysis of peak height, peak width, and peak location would be required before making claims about an asymptotic limit.

Future work should therefore focus on direct basin mapping, targeted perturbation experiments, and analytical reductions of the normalized field dynamics. Because the field is separable into row and column components, the SFCA may admit lower-dimensional descriptions based on row and column densities. Such reductions could help explain why the transition boundary is sharp and why stripe-like attractors become stable after the persistence band widens.

5. Conclusion

We introduced a normalized separable-field cellular automaton and showed that its long-term dynamics are organized by the geometry of survival and birth intervals. Across parameter space, the SFCA produces extinction,

fixed points, cycles, and long transients, with each outcome occupying structured regions rather than appearing as isolated exceptions. Fixed points are enriched when the birth interval is contained within the survival interval, whereas long transients concentrate near the boundary between partial overlap and no overlap.

Along a fine transition scan, the long-transient ridge separates two distinct cyclic attractor families: a dense, high-change-rate cycle basin and a sparse, stripe-like, low-change-rate cycle basin. Cycle fingerprints and damage-spreading analyses support a basin-competition interpretation, in which long transients arise from delayed selection between these cyclic attractor families rather than from unstructured randomness. Finite-size analysis further shows that the long-transient ridge persists across tested grid sizes, suggesting that the observed transition structure is not a small-system artifact.

Together, these results establish the SFCA as a compact model for studying how normalized global fields and interval geometry can generate structured metastability under compressed interaction architecture. More broadly, they suggest that nontrivial long-transient organization can arise without conventional local-neighborhood combinatorics.

Data and code availability

The simulation code and analysis scripts used in this study are publicly available on GitHub at `https://github.com/huangmengs/SFCA.git`. Generated figures and processed outputs can be reproduced from the repository and the parameter settings described in this manuscript.

Competing interests

The authors declare no competing interests.

References

Crutchfield, J.P., Kaneko, K., 1988. Are attractors relevant to turbulence? Physical review letters 60, 2715.

Gardner, M., 1970. Mathematical games. Scientific american 222, 132–140.

JD, F., 1986. Autocatalytic replication of polymers. Physica D .

Kauffman, S.A., 1986. Autocatalytic sets of proteins. Journal of theoretical biology 119, 1–24.

Mayzel, J., Schneidman, E., 2024. Homeostatic synaptic normalization optimizes learning in network models of neural population codes. Elife 13, RP96566.

Mordvintsev, A., Randazzo, E., Niklasson, E., Levin, M., 2020. Growing neural cellular automata. Distill 5, e23.

Pajouheshgar, E., Xu, Y., Abbasi, A., Mordvintsev, A., Jakob, W., Süsstrunk, S., 2025. Neural cellular automata: From cells to pixels. arXiv preprint arXiv:2506.22899 .

Parres-Gold, J., Levine, M., Emert, B., Stuart, A., Elowitz, M.B., 2025. Contextual computation by competitive protein dimerization networks. Cell 188, 1984–2002.

Wolfram, S., 1984. Cellular automata as models of complexity. Nature 311, 419–424.

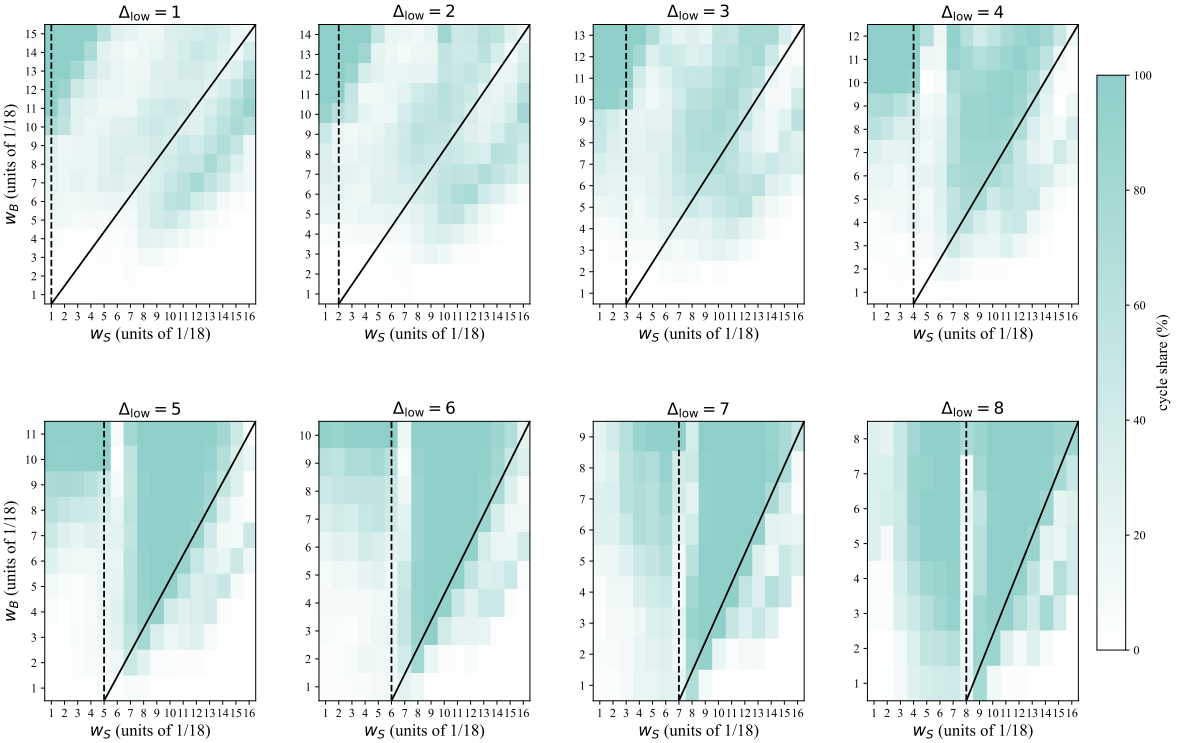

Figure 1: Cycle phase map on the $S_{width} \times B_{width}$ plane with Δ_{low} varying from 1/18 to 8/18. Black dashed line: $B_{low} = S_{high}$; black solid line: $B_{high} = S_{high}$. Maximum generation = 2000. Parameters: $S_{low} = 1/18, B_{low} = 6/18$, 2000 generations per run, 100 random initial conditions per parameter set, initial density 0.25.

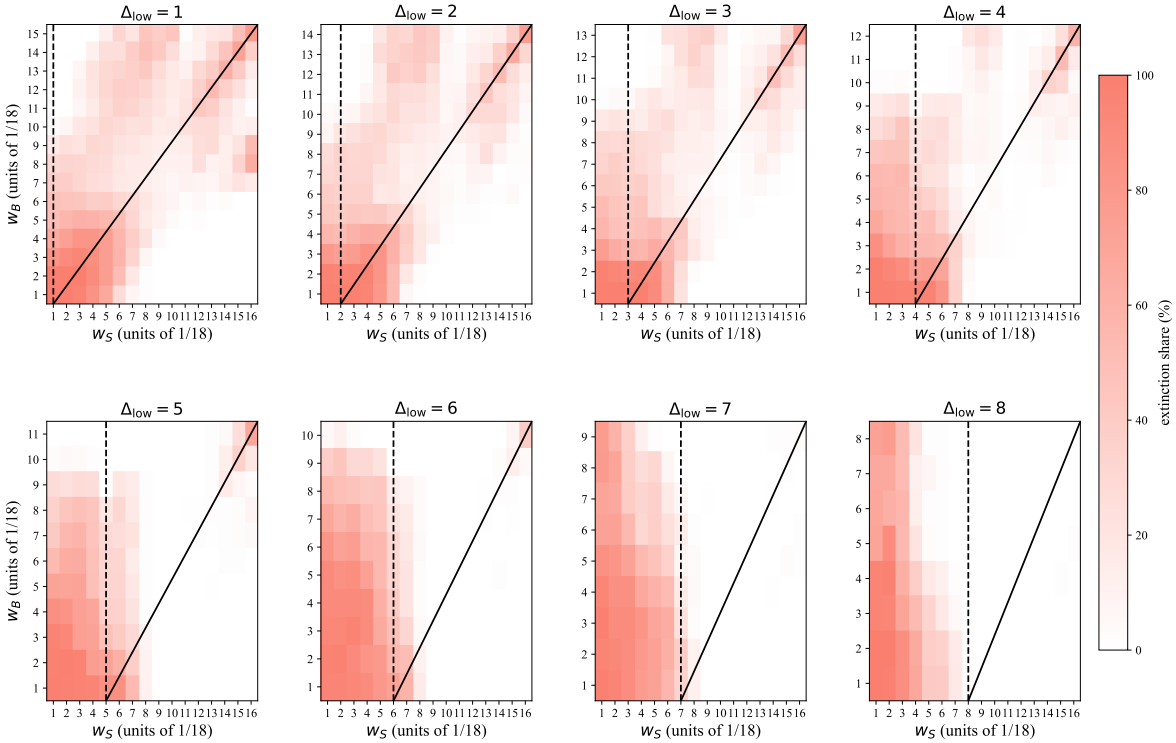

Figure 2: Extinction phase map on the $S_{width} \times B_{width}$ plane with Δ_{low} varying from 1/18 to 8/18. Black dashed line: $B_{low} = S_{high}$; black solid line: $B_{high} = S_{high}$. Parameters: $S_{low} = 1/18, B_{low} = 6/18$, 2000 generations per run, 100 random initial conditions per parameter set, initial density 0.25.

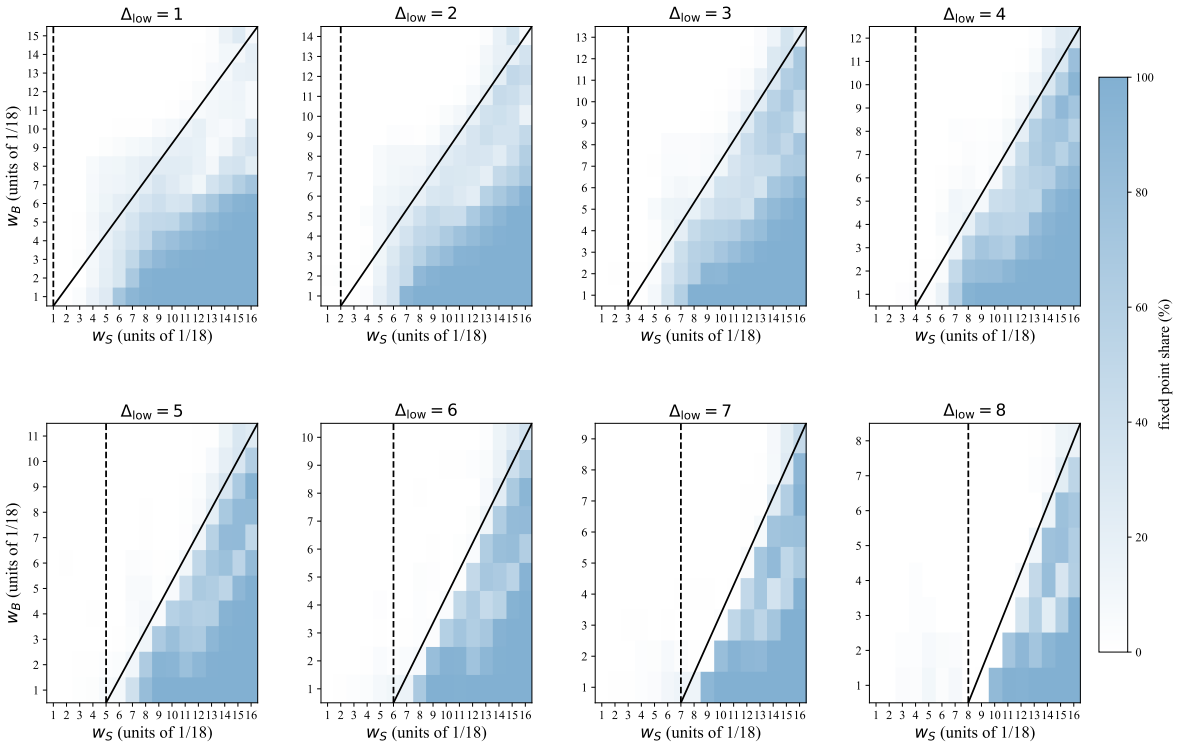

Figure 3: Extinction phase map on the $S_{width} \times B_{width}$ plane with Δ_{low} varying from 1/18 to 8/18. Black dashed line: $B_{low} = S_{high}$; black solid line: $B_{high} = S_{high}$. Parameters: $S_{low} = 1/18, B_{low} = 6/18$, 2000 generations per run, 100 random initial conditions per parameter set, initial density 0.25.

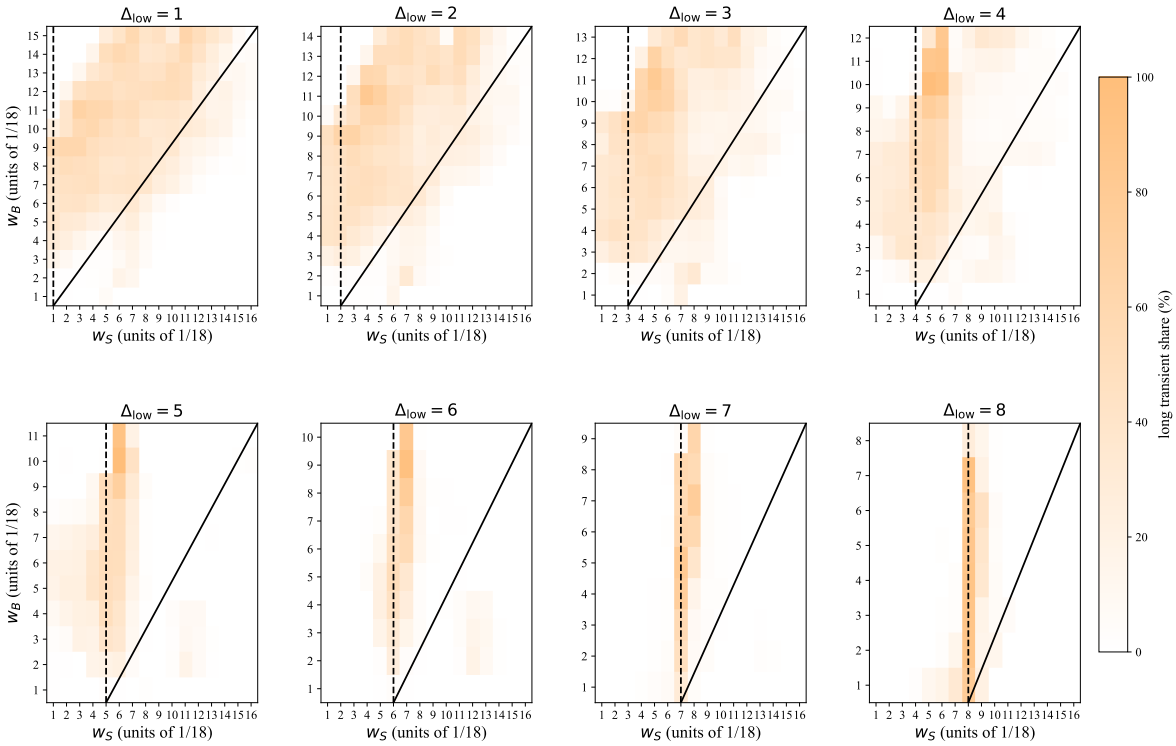

Figure 4: Long transient phase map on the $S_{width} \times B_{width}$ plane with Δ_{low} varying from 1/18 to 8/18. Black dashed line: $B_{low} = S_{high}$; black solid line: $B_{high} = S_{high}$. Parameters: $S_{low} = 1/18, B_{low} = 6/18$, 2000 generations per run, 100 random initial conditions per parameter set, initial density 0.25.$B_{low} = S_{high}$

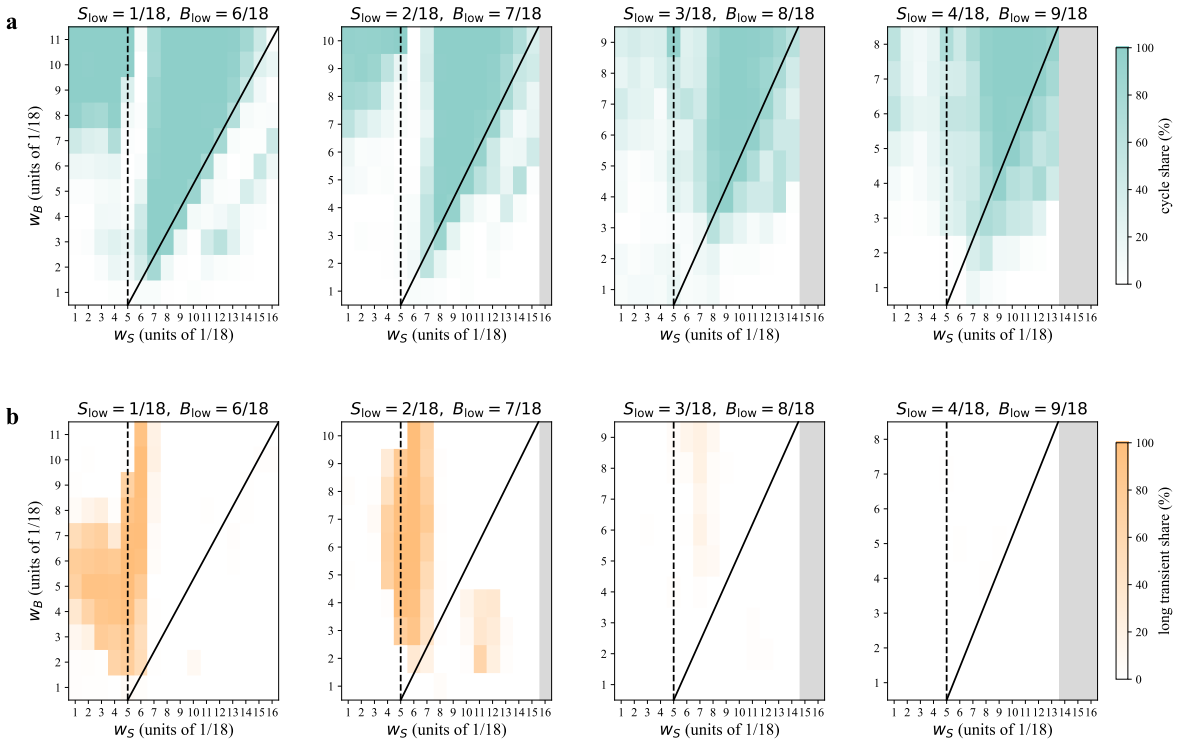

Figure 5: (a) Cycle phase map on the $S_{width} \times B_{width}$ plane when $\Delta_{low} = B_{low} - S_{low} = 5/18$, and S_{low} vary from 1/18 to 4/18. Black dashed line: $B_{low} = S_{high}$; black solid line: $B_{high} = S_{high}$. Parameters: 2000 generations per run, 100 random initial conditions per parameter set, initial density 0.25. (b) Long transient phase map on the $S_{width} \times B_{width}$ plane when $\Delta_{low} = B_{low} - S_{low} = 5/18$, and S_{low} vary from 1/18 to 4/18. White dashed line: $B_{low} = S_{high}$; white solid line: $B_{high} = S_{high}$. Parameters: 2000 generations per run, 100 random initial conditions per parameter set, initial density 0.25.

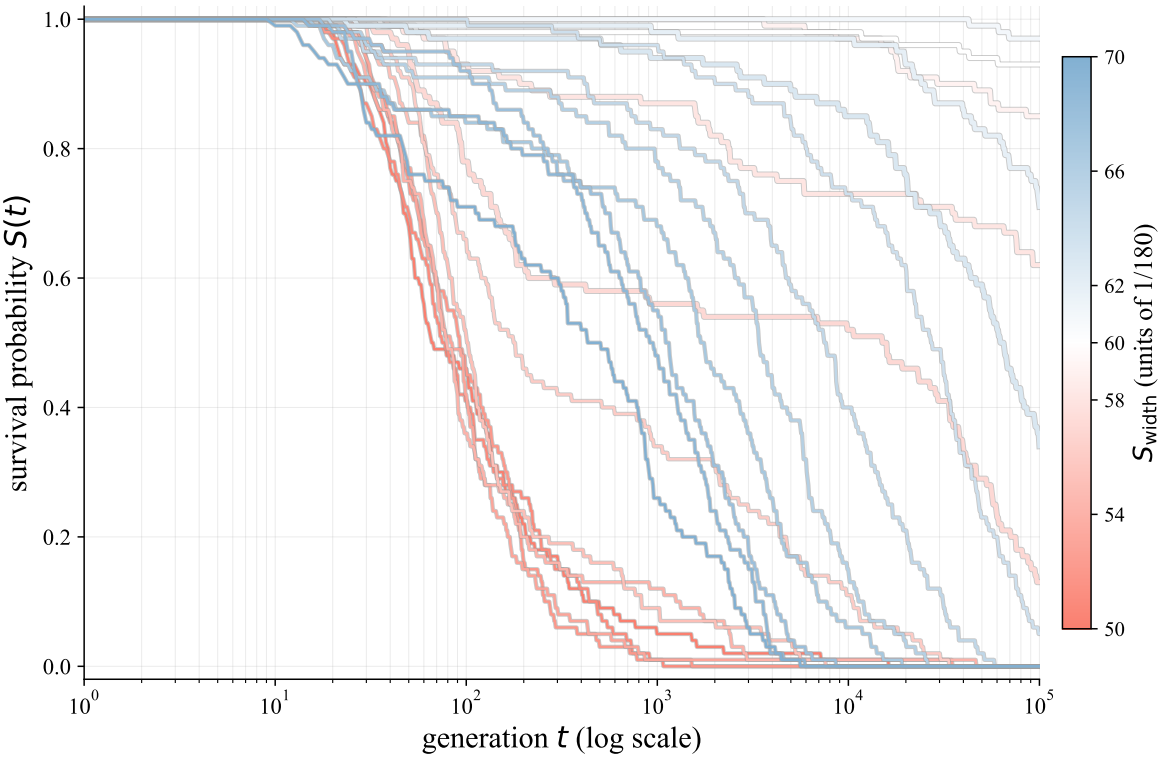

Figure 6: Kaplan-Meier survival curves of transient lifetime across S_{width}. Survival probability S(t) = P(τ > t) : the fraction of trajectories that have not yet converged to a detectable attractor (extinction, fixed point, or periodic cycle) by generation t - is shown for 21 values of S_{width} from 50/180 to 70/180. Each curve is computed from 100 independent runs using the Kaplan-Meier estimator, with right-censored trajectories (those classified as long transient at the end of the observation window) contributing to S(t) for all $t \leq 100,000$. In the ordered regimes ($S_{width} \leq 56/180 and \geq 64/180$), survival probability drops rapidly to zero, indicating that nearly all trajectories converge within the first few thousand generations. In the critical zone (S_{width} = 57-63), survival curves plateau at elevated levels (up to $S \approx 0.97$ for S_{width} = 60) and persist without further decay to the end of the observation window, demonstrating that the majority of trajectories remain in a non-convergent long-transient state for at least 100,000 generations. Parameters: 100×75 grid, S_{low} = 1/18, B_{low} = 6/18, B_{high} = 16/18, B_{width} = 10/18, initial density 0.25, Δ_{low} = 5/18.

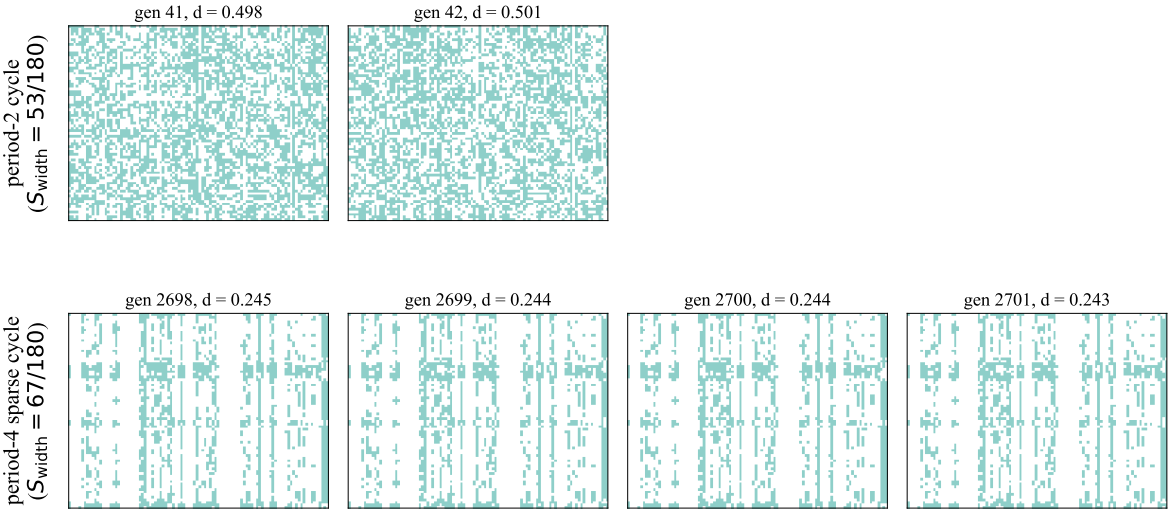

Figure 7: Representative dense and sparse cycle trajectories on opposite sides of the long-transient region in the phase map. A typical dense cycle was selected from the parameter region on the left side of the long-transient band in the S_{width}–B_{width} phase map, whereas a typical sparse cycle was selected from the parameter region on the right side. For each trajectory, all phases of the detected cycle are shown, illustrating that the two cycle-dominated regions separated by the long-transient band correspond to qualitatively distinct periodic spatial organizations.

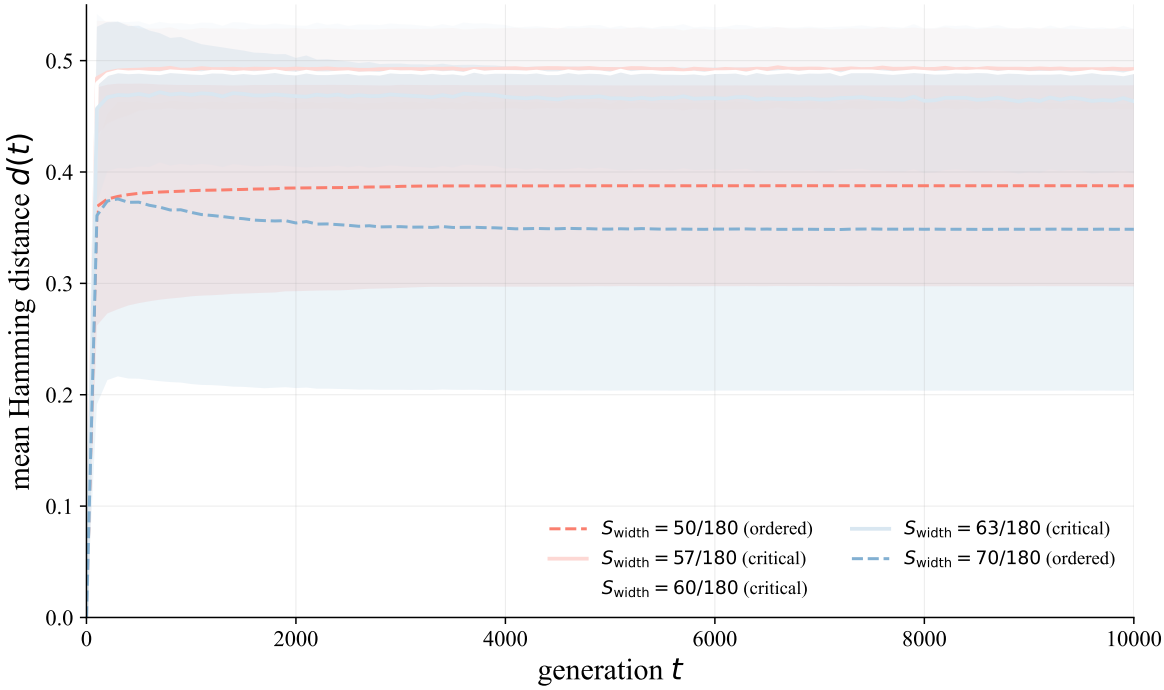

Figure 8: Mean perturbation propagation distance d(t) over time. The Hamming distance between two initially identical 100×75 grids differing by a single flipped cell is shown as a function of generation t, averaged over 500 independent pairs per S_{width} value. Solid curves correspond to critical-zone parameters ($S_{width} = 57/180$–$63/180$); dashed curves correspond to ordered-regime parameters ($S_{width} = 50/180, 70/180$). Shaded ribbons indicate ± 1 standard deviation. Parameters: $S_{low} = 1/18$, $B_{low} = 6/18$, $B_{high} = 16/18$, $B_{width} = 10/18$, grid size 100×75, 100,000 generations per run, initial density 0.25.

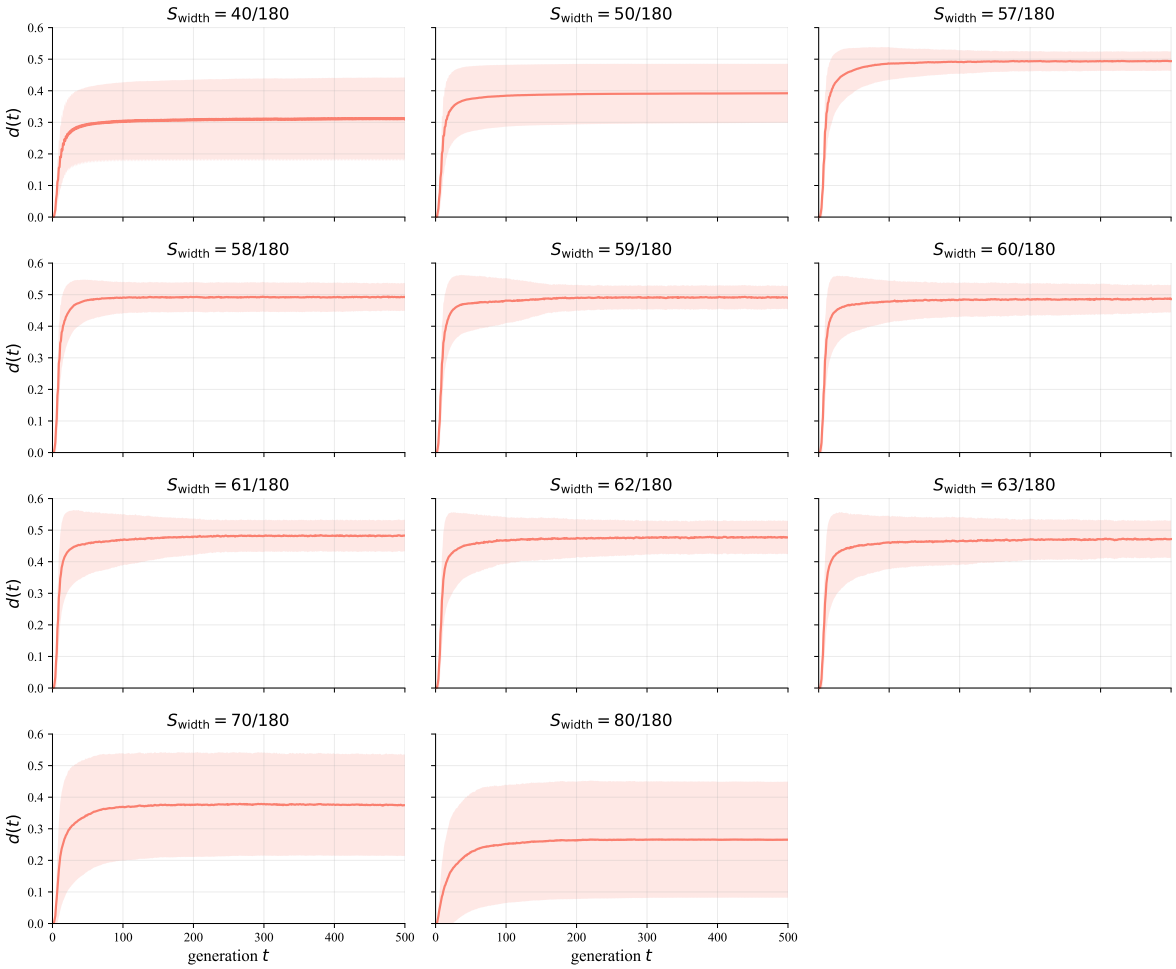

Figure 9: High-resolution early-time perturbation propagation d(t) for 11 S_{width} values. Each panel shows the Hamming distance d(t) between two initially identical grids differing by a single flipped cell, recorded every generation for the first 500 generations. Solid curves represent the mean across 500 independent runs; shaded ribbons indicate ± 1 standard deviation. Parameters: $S_{low} = 1/18$, $B_{low} = 6/18$, $B_{high} = 16/18$, $B_{width} = 10/18$, $\Delta_{low} = 5/18$, grid size 100×75, 500 generations per run, 500 random initial conditions per parameter set, initial density 0.25.

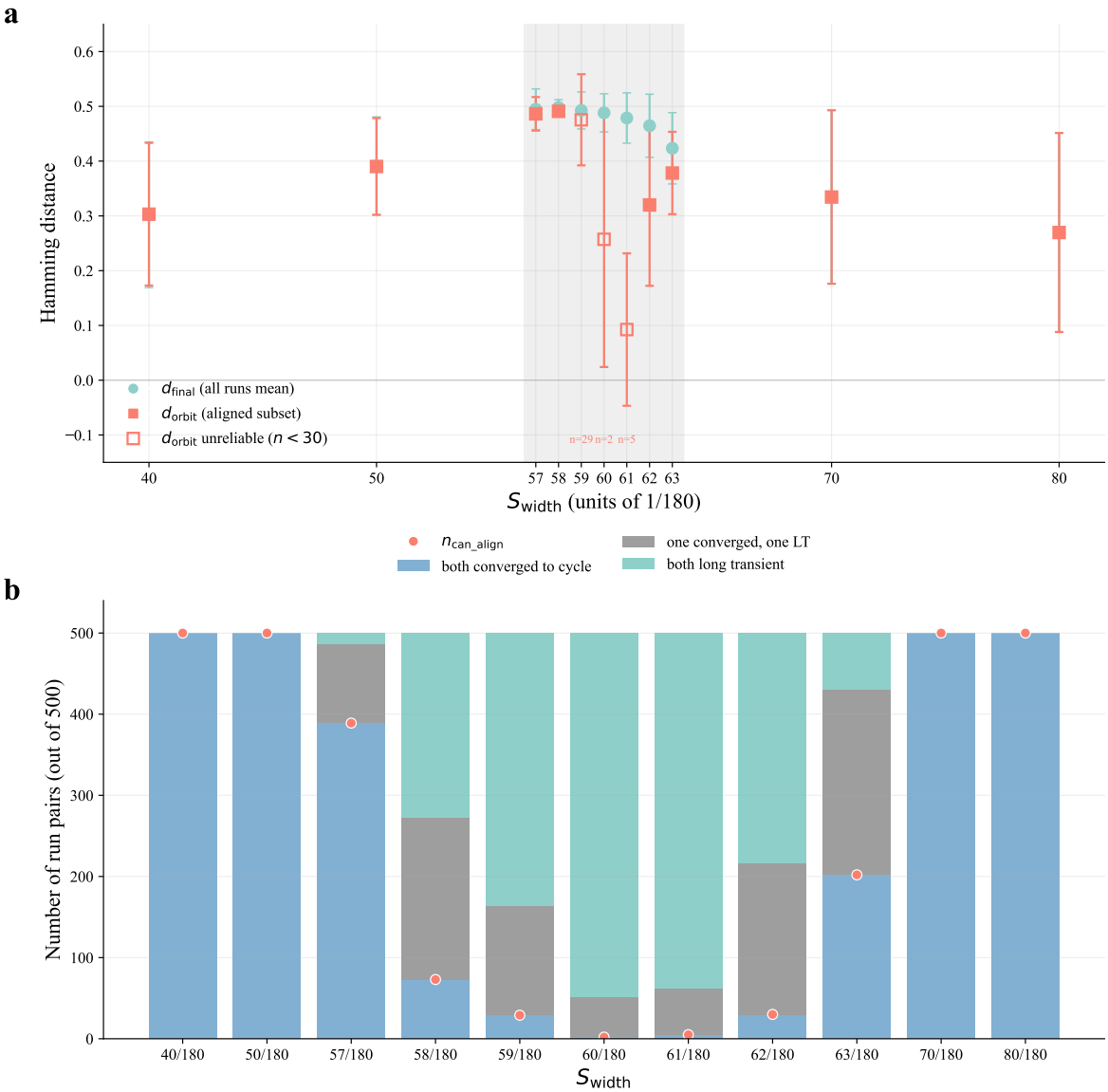

Figure 10: (a) d_{final} and d_{orbit} across S_{width}. The open circles show the mean final Hamming distance d_{final} averaged over all 500 runs per S_{width} (including both long-transient and converged trajectories). The solid squares show d_{orbit} - the phase-aligned minimum Hamming distance computed only from the subset of run pairs where both the reference and the perturbed grid converged to a detectable cycle and the cycle length was $\leq$ 10,000 generations. Error bars indicate ± 1 standard deviation. Hollow markers indicate S_{width} values where fewer than 30 run pairs could be aligned, making the d_{orbit} estimate unreliable due to selection bias. The grey shaded region highlights the long-transient-dominated zone ($S_{width} = 57/180 - 63/180$), where d_{orbit} is largely unavailable because fewer than 6% of runs converged. Where reliable data exist ($S_{width} \leq 58/180$ and $\geq 62/180$), d_{orbit} closely tracks d_{final} (the gap never exceeds 0.02), demonstrating that the apparent differences between the two grids are almost entirely due to genuine structural divergence rather than mere phase shifts along the same periodic orbit. Parameters: $S_{low} = 1/18$, $B_{low} = 6/18$, $B_{high} = 16/18$, $B_{width} = 10/18$, $\Delta_{low} = 5/18$, grid size 100×75, 500 generations per run, 500 random initial conditions per parameter set, initial density 0.25. (b) Breakdown of convergence outcomes across S_{width}. Stacked bars show the classification of the 500 run pairs per S_{width} into three mutually exclusive categories - both the reference and perturbed grids converged to a detectable cycle; one grid converged while the other remained in long transient; both grids remained in long transient for the full 100,000-generation observation window.

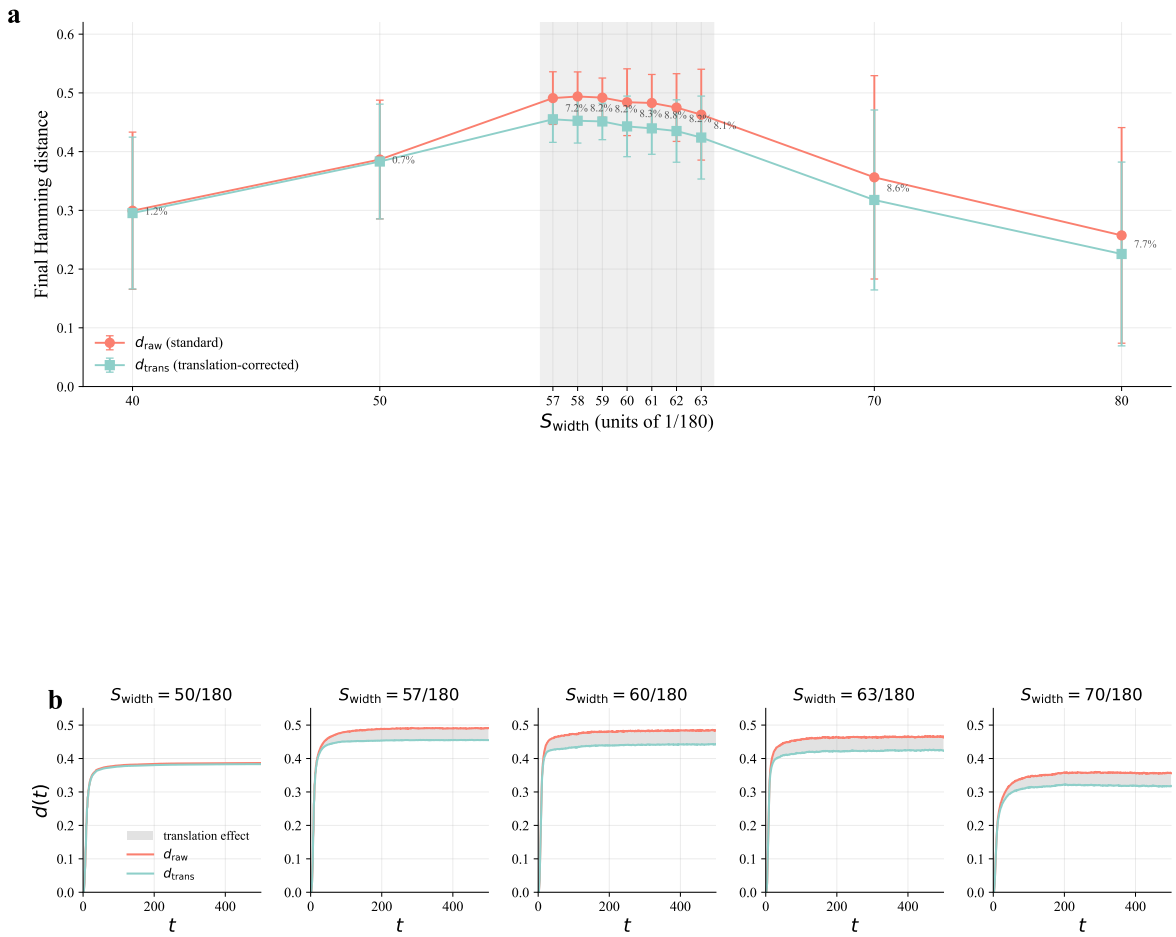

Figure 11: (a) Standard and translation-corrected final Hamming distance across S_{width}. The red circles show d_{raw} — the conventional final Hamming distance d_{final} averaged over 500 run pairs per S_{width}. The teal squares show d_{trans} — the Hamming distance computed after optimally shifting one grid relative to the other via 2D FFT cross-correlation to minimise spatial translational offsets. Error bars indicate ± 1 standard deviation. Numeric labels between the two curves indicate the per-run mean translation effect ratio $1 - d_{trans}/d_{raw}$ as a percentage. The grey shaded region highlights the long-transient-dominated zone ($S_{width} = 57/180 - 63/180$). The translation correction reduces the measured distance by 8% across the overlapping-window regime ($S_{width} \geq 57/180$) and by less than 2% in the fully separated regime ($S_{width} \leq 50/180$). The remaining 92% of d_{raw} is attributable to genuine structural differences rather than translational symmetries. Parameters: $S_{low} = 1/18, B_{low} = 6/18, B_{high} = 16/18, B_{width} = 10/18, \Delta_{low} = 5/18$, grid size 100×75, 500 generations per run, 500 random initial conditions per parameter set, initial density 0.25. (b) Time evolution of $d_{raw}(t)$ and $d_{trans}(t)$ for selected S_{width} values. The Hamming distance $d(t)$ is shown for both the standard measurement (red) and its translation-corrected counterpart (teal), averaged over 500 run pairs per S_{width}. The grey shaded area between the two curves represents the fraction of the apparent divergence attributable to spatial translation. Parameters: $S_{low} = 1/18, B_{low} = 6/18, B_{high} = 16/18, B_{width} = 10/18, \Delta_{low} = 5/18$, grid size 100×75, 500 generations per run, 500 random initial conditions per parameter set, initial density 0.25.

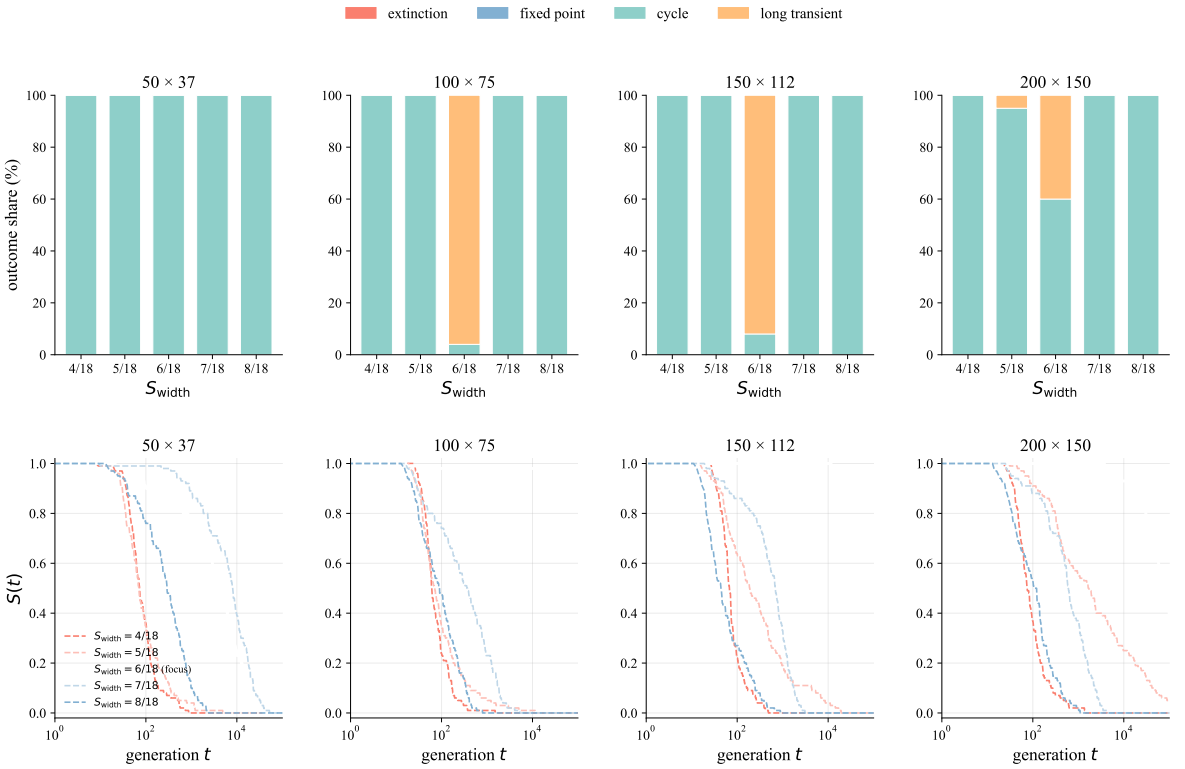

Figure 12: Finite-size scaling of outcome composition and transient lifetime. Top row: stacked bar charts showing the proportion of 100 independent runs classified into four dynamical outcomes (extinction, fixed point, cycle, long transient) for four grid sizes - (a) 50×37, (b) 100×75, (c) 150×112, and (d) 200×150 - as a function of S_{width} (units of 1/18). Each bar represents 100 runs at 100,000 generations per run. Bottom row (e) Kaplan-Meier survival curves $S(t) = P(\tau > t)$ at $S_{width} = 6/18$ for the same four grid sizes, showing the fraction of trajectories not yet converged by generation t. Parameters: $S_{low} = 1/18, B_{low} = 6/18, B_{high} = 16/18, B_{width} = 10/18, \Delta_{low} = 5/18$, 100,000 generations per run, 100 random initial conditions per parameter set, initial density 0.25.

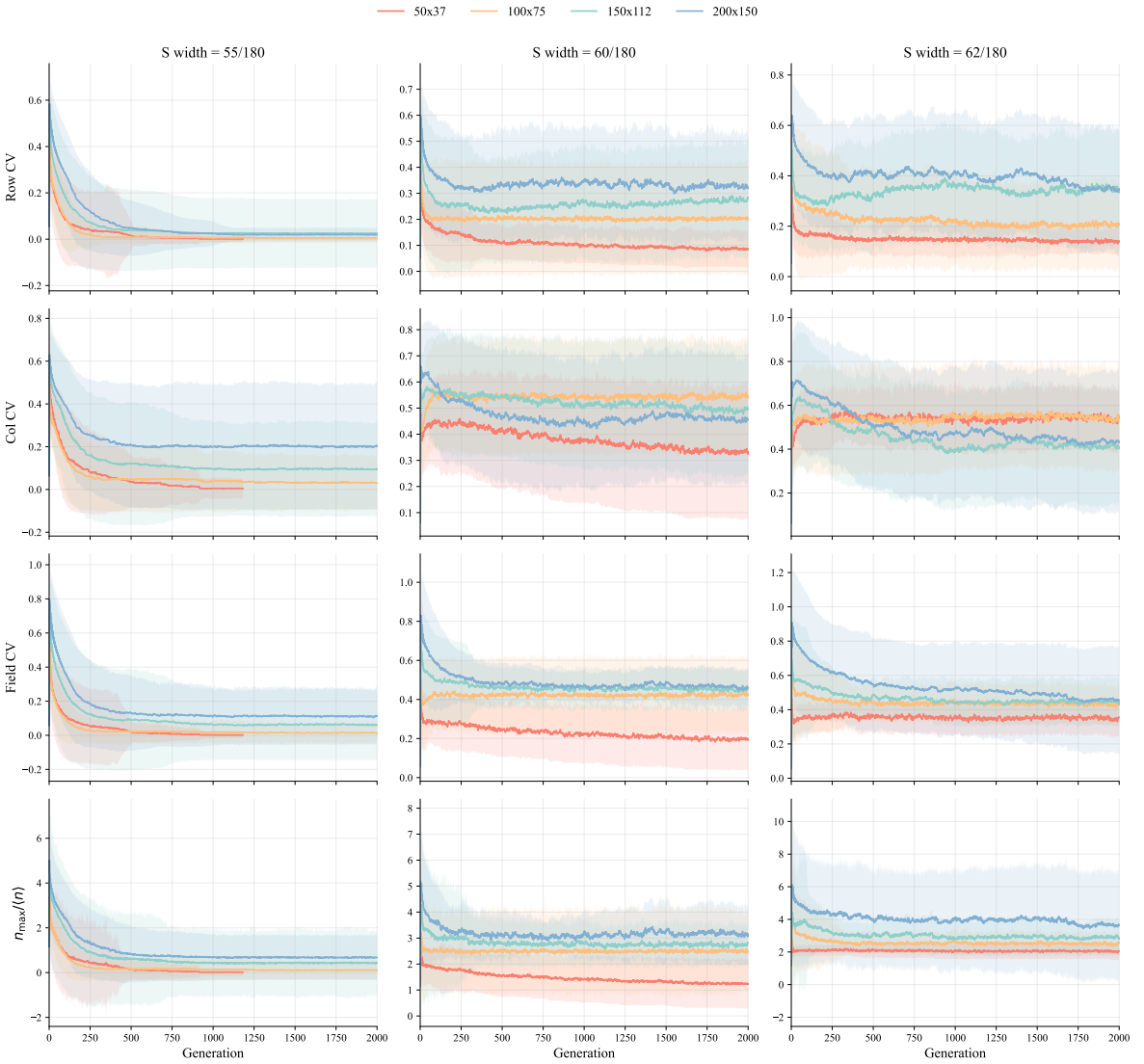

Figure 13: Field-statistics evolution across grid sizes at three S_{width} values. The four rows show (from top to bottom) Row CV, Column CV, Field CV, and $n_{max}/\langle n \rangle$ ratio as functions of generation t up to 2000 generations. The three columns correspond to S_{width} = 55/180, 60/180, and 62/180. Each coloured curve represents the mean over 100 independent runs for a given grid size (50 × 37, 100 × 75, 150 × 112, 200 × 150); shaded ribbons indicate ±1 standard deviation. Parameters: $S_{low} = 1/18, B_{low} = 6/18, B_{high} = 16/18, B_{width} = 10/18, \Delta_{low} = 5/18$, 2000 generations per run, 100 random initial conditions per parameter set, initial density 0.25.